Convection initiation at a coastal rainfall hotspot in South China: Synoptic patterns and orographic effects

Lanqiang Bai [1,2], Guixing Chen *[2], Yipeng Huang [3], and Zhiyong Meng [4]

[1] *Foshan Tornado Research Center, Foshan Meteorological Service, Foshan, China*

[2] *School of Atmospheric Sciences, Sun Yat-sen University, and Southern Marine Science and Engineering Guangdong Laboratory (Zhuhai), Zhuhai, China*

[3] *Xiamen Key Laboratory of Straits Meteorology, Xiamen Meteorological Bureau, Xiamen, China*

[4] *Department of Atmospheric and Oceanic Sciences, School of Physics, Peking University, Beijing, China*

Revised version for *Journal of Geophysical Research: Atmospheres*, October 2021

* Corresponding author: Dr. Guixing Chen (chenguixing@mail.sysu.edu.cn)

ORCID:

0000-0002-0304-5656 (Lanqiang Bai)
0000-0002-3112-0668 (Guixing Chen)
0000-0002-5344-9130 (Yipeng Huang)
0000-0002-2527-1056 (Zhiyong Meng)

Article Highlights:

- The genesis of warm-season convection at a rainfall hotspot in South China preferentially occurs near the coastal orography.
- The characteristic low-level onshore southwesterlies in monsoon flows are the dominant synoptic pattern favorable for the coastal CI.
- Coastal small mountains may generate substantial local variations in the lifting and moisture pooling, determining the detailed CI pattern.

Abstract

This study documents the detailed features and processes of convection initiation (CI) at a coastal rainfall hotspot in South China, with emphasis on the typical meteorological conditions and effects of small-scale orography. The CI occurrences are identified using high-quality radar mosaics during 7-yr warm seasons. They tend to maximize in low-lying areas adjacent to coastal small-scale mountains rather than on the windward slopes of major mountains as previously expected. The genesis of the coastal convection exhibits a remarkable diurnal peak in the early afternoon and mostly occurs on the days of low-level southwesterlies with a jet-nose structure in offshore region. These onshore flows enhance the low-level moistening and convergence on coasts. The characteristic synoptic patterns become common after the onset of summer monsoon, suggesting the key role of monsoonal flows in triggering coastal convection. Driven by the atmospheric conditions of the dominant synoptic pattern, quasi-idealized numerical simulations demonstrate that the coastal small-scale mountains disturb the low-level onshore flow and produce multiple enhanced convergent zones downstream of the mountains. The induced local variations in upward motion and moisture pooling explain the CI occurrences that are located close to these small-scale mountains. When these mountains are artificially removed in the simulation, convection preferentially initiates on the windward slopes of major mountains as expected. The findings suggest that the small-scale orography can strongly regulate the local patterns of CI hotspot through disturbing low-level onshore flow. An explicit resolving of such local coastal orography is warranted to improve the modeling of local severe weather.

1. Introduction

Deep moist convection and the associated rainfall frequently occur on global coasts, especially on the windward sides of coastal orography in monsoon regions, playing a vital role in energy and hydrologic cycles (Xie et al., 2006; Chen et al., 2018). They threaten the public safety and property with flash floods, high winds, lightning, hail and occasionally tornadoes. The genesis of convection, namely convection initiation (CI), is one of the most important issues in quantitative precipitation forecast because rainfall strongly depends on the timing and location of CI. The improved understanding and prediction of CI in coastal areas are thus integral parts of the disaster prevention and mitigation for severe weather.

CI has long been known to be a result of the interaction of multiscale atmospheric processes which contributes to the locally enhanced lifting and moisture pooling. Here the moisture pooling indicates the development of an area in the planetary boundary layer (PBL) where moisture values become higher than in the surrounding region (American Meteorological Society, 2021). The synoptic-scale circulation often primes the mesoscale environment for CI by large-scale mean ascent, moistening the atmosphere and thus increasing the convective instability (Markowski & Richardson, 2010). Local convergent zones in the PBL usually play a crucial role in triggering convection primarily by the forced lifting. The common enhanced PBL lifting is often located on mesoscale boundaries, such as gust fronts, drylines, surface wind shift lines, sea-breeze fronts, gravity waves, and horizontal convective rolls (e.g., Saito et al., 2018; Wilson & Roberts, 2006, and references therein). These boundaries can be identified by a variety of observational platforms and are carefully assessed by forecasters to help the CI nowcasting.

In addition to the PBL convergent boundary, orography is also a key factor for triggering convection. The resultant convection often repeatedly initiates in the region with some particular topographical features rather than more or less random as in flat areas (Banta & Schaaf, 1987). The orography-related dynamics such as mechanical

orographic forcing, leeside convergence, channeling, wake effects, and mountain waves are supportive of the formation of convection (Banta & Schaaf, 1987; Markowski & Richardson, 2010). The differential heating between mountains and surrounding plains also induces a solenoidal circulation (mountain-plains solenoid), which leads to a diurnal variation in the spatial distribution of active convection area (Chen et al., 2016). The aforementioned orography-induced disturbances to the ambient flow suggest a possible spatial dependence of convection triggering on given regional topographical features. Identifying the topographical features that repeatedly stimulate the genesis of convection may thus aid in the regional thunderstorm prediction. The CI-preferred topographical features also depend on the direction and strength of low-level ambient flows (Banta & Schaaf, 1987; Schaaf et al., 1988; Xie et al., 2006; Chen et al., 2016). It is thus important to identify the dominant synoptic background flow that regulates the local circulations in given mountainous regions, thereby determining the detailed patterns of CI over there.

Some synoptic features such as low-level jets (LLJs) may also support the genesis of convection. Reif and Bluestein (2017) documented that over 70% of their identified CI events were characterized by a nearby LLJ signature. These CI events tended to occur on the eastern side of the north–south-orientated LLJs, suggesting a dependence of CI location on the cross-axis heterogeneity of LLJ. In the presence of an LLJ, the associated moisture transport may contribute to the formation of a moist absolutely unstable layer (MAUL) that is conducive to CI (Geerts et al., 2017; Trier et al., 2017; Shapiro et al., 2018; Zhang et al., 2019). LLJs also benefit the deepening of moist layer by the enhanced convergence and lifting. The terminus of an LLJ with enhanced horizontal convergence is often the CI-prone region (Chen et al., 2014; Gebauer et al., 2018; Du & Chen, 2019a,b). The intersection of an LLJ with other atmospheric boundaries (e.g., fronts and outflow boundaries) is also favorable for CI by enhancing mesoscale lifting (Trier et al., 2017).

The coastal regions of South China witness the most active convection in China, especially after the onset of the East Asian summer monsoon (Zhang et al., 2017; Luo et al., 2017, 2020). The orographic effects and the convergence between land breezes/downslope winds and low-level onshore flows (especially the onshore marine LLJ) play an important role in the regional hydrologic cycle (Luo et al., 2020; Wang et al., 2021; Bao et al., 2021). The CI occurrences in this region are pronounced from June to August, with a primary peak in the early afternoon and a secondary peak at midnight (Bai et al., 2020a). They are primarily concentrated within 100 km of the coastline with local maxima around coastal orography. One of the local maxima in CI occurrence is located in the Yangjiang region (refer to the blue box in Figure 1a) on the western coast of Guangdong Province. This area is also one of the climatological rainfall centers where the annual rainfall accumulation can reach 2200 mm (refer to the colored dots in Figure 1a; Luo et al., 2017; Wu et al., 2020). During the warm seasons, the Yangjiang region is dominated by short-duration convective rainfall on land in the afternoon and the long-duration rainfall on coastlines in the morning (Chen et al., 2018; Li et al., 2019). Case studies also showed that the presence of so-called "double LLJs" in the coastal region may encourage CI (refer to Figure 21 in Du & Chen, 2019a; Liu et al., 2020). The low-level convergence and higher-level divergence in such an ambient wind profile produce a favorable dynamic structure for low-level lifting. It is our impression that the quantitative precipitation forecast (QPF) failure often results from an inability in anticipating CI and the associated LLJs (Zhang & Meng, 2018, 2019), especially for the afternoon convection. Considering that the Yangjiang region is a hotspot of convection and rainfall, improving our knowledge on the CI characteristics and associated physical processes over there is important for scientific understanding and operational forecast.

This study aims to clarify the detailed features and associated processes of the convection triggering in the Yangjiang region. The characteristics of CI occurrences identified from long-term radar observations and the objectively identified synoptic

conditions favorable for CI are first presented. Quasi-idealized convection-permitting simulations were then conducted under the dominant synoptic pattern to illustrate how the local circulations near coastal orography determine the detailed CI patterns.

2. Data and Methods

The CI occurrences in the region of interest were obtained from the CI climatology in South China that was compiled during the warm seasons (April–September) from 2013 to 2019 using high-quality radar mosaics (Bai et al., 2020a). These CI events tend to represent the isolated convective storms that are not associated with existing precipitation systems. For more details regarding the CI identification, please refer to Bai et al. (2020b). The radar mosaics were available every 10 min before June 2016 and every 6 min afterward. Some short-lived convection may be missed at a longer time interval of data availability, leading to a relatively smaller sample size of CI occurrence in the earlier years. For this reason, the annual variation of CI occurrence is not discussed in the current study. To investigate the possible link of the local rainfall to CI in the region of interest, the multi-satellite merged rainfall estimates from the NOAA Climate Prediction Center morphing technique (CMORPH v1.0) were used. These data were derived by an optimal combination of high-quality microwave rainfall estimates and geostationary infrared rainfall estimates and are available every 30 min at a horizontal resolution of 8 km (Joyce et al., 2004; Huffman et al., 2007). They have been demonstrated to be able to well resolve the fine patterns of rainfall on the coasts of South China (Chen et al., 2018).

The topography data used for analysis and numerical simulation were derived from the global 30 arc-second elevation dataset (GTOPO30) produced by the Earth Resources Observation Systems (EROS) Data Center of the United States Geological Survey (USGS). The small-scale coastal mountains of interest (labeled M2 and M3) are located to the south of the major mountain M1 (Figure 1b). The mountains M2 and M3 are relatively isolated obstacles with a small horizontal scale. The maximum horizontal

lengths of the topography above 250 m altitude for the mountains M2 and M3 are approximately 32 km and 11 km, respectively. These two mountains are characterized by a peak height of 1134 m and 693 m (Figure 1b).

The large-scale circulations were objectively classified by the obliquely rotated principal component analysis (PCA) in T mode (PCA-T hereinafter; Huth, 1996, 2000). Previous studies have suggested a reasonablly good performance of the PCA-T in the synoptic-pattern classification in South China (Rao et al., 2019; Wang et al., 2021). The identified typical synoptic patterns are thus helpful in investigating the most prominent interaction (favoring CI) between background airflows and regional forcings such as coastal orography. To conduct the PCA-T analysis, the open source software package "cost733class" within the framework of COST Action 733 "Harmonisation and Applications of Weather Type Classifications for European Regions" (Philipp et al., 2016) was used. The fifth generation of ECMWF atmospheric reanalysis (ERA5) data were used as the input data for the PCA-T analysis, which are hourly available at a horizontal resolution of 0.25° (Hersbach et al., 2020). The ERA5 reanalysis data were also used to identify the existence of LLJ following the criteria proposed by Du & Chen (2019b): 1) the maximum wind speed below 700 hPa is greater than 10 m s^{-1}, and 2) the difference between this maximum speed and the minimum speed from the maximum speed level to 600 hPa is no less than 3 m s^{-1}.

3. Climatology of CI occurrence and associated synoptic conditions

a. Temporal and spatial distributions of CI occurrence

During April–September from 2013 to 2019, a total of 849 CI events were identified in the Yangjiang area (within the blue box in Figure 1a). The CI occurrences increase evidently from April to June, reach the maximum in July, and decrease afterward (Figure 2a). On a shorter timescale, the CI activity presents an evident diurnal

variation in terms of both the occurrence frequency (Figure 2b) and spatial pattern (Figure 3). Up to 64% of the CI occurrences take place in the daylight hours (0700–1900 LST; LST=UTC+8h) with a remarkable increase from 1100 LST and a diurnal peak at 1400 LST (Figure 2b). Approximately 49% of the CI occurrences take place during the hours from 1100 to 1700 LST. A secondary CI peak occurs at 0300 LST, which may be attributed by the cloud-top radiative cooling that accelerates condensation and the enhanced low-level convergence between onshore flows and land breezes or downslope winds (Chen et al., 2016; Bai et al., 2020a).

The maxima in daytime CI occurrence are located on the relatively flat land rather than on the slopes of the major mountain M1 (Figure 3b). Specifically, CI is particularly active in the low-lying area surrounded by the four mountains M1–M4. The CI occurrences are maximized in the region in close proximity to the mountains M2 and M3, although they also preferentially occur on the southern slopes of the mountain M1. During the nighttime (1900–0700 LST), CI occurrences are concentrated on coastlines and in offshore regions (Figure 3c). Such evidently different spatial modes of CI may be indicative of quite different physical mechanisms of nocturnal convection triggering in contrast to that in the daytime. Given that the coastal land in this region is dominated by afternoon rainfall (Chen et al., 2018) and that a majority of CI occurs during the daytime, we primarily focus on the daytime CI and its associated triggering mechanisms in this study.

In this climatological rainfall center, rainfall is typically contributed by locally triggered storms, propagating storms from nearby regions, or long-lived precipitation systems caused by strong synoptic forcings such as quasi-stationary fronts and tropical cyclones. With the aid of CI database, the rainfall related to the locally triggered convection can be estimated. In this study, the hourly available CMORPH rainfall data were used to estimate the rainfall amount that possibly owes to the local CI process. Because the precipitation systems in the target area may evolve from substantial secondary generation of convection (namely secondary CI that is strongly influenced

by existing convection), we did not track each CI associated convective cell. Given that the duration of afternoon convective rainfall is typically shorter than 6 h (Yu et al., 2007; Chen et al., 2018), we may regard the domain rainfall accumulation within 6 h after the CI onset as the rainfall proxy that is directly related to the locally triggered storms. In this scenario, approximately 17% of the rainfall amount during the warm season is produced by the locally triggered convection in the Yangjiang area. Figure 2c shows that the domain-average rainfall rate undergoes a significant increase after the onset of CI and reaches a maximum 5–6 h later. The average rainfall intensity during the 4–8 h after CI appears to be 30% higher than that of the climatological mean. These high-intensity rainfall with a relatively long duration may suggest that some of the locally triggered storms grow upscale into organized convective systems in about 4 h. Therefore, the rainfall amount directly due to the locally triggered storms is an important component of the hydrologic cycle in this coastal rainfall hotspot.

b. Synoptic patterns on CI days

The objective classification for the synoptic patterns on CI days is presented in this section. Here a CI day is defined as the day when there was at least one CI event during 0700–1900 LST. There was a total of 466 CI days in the Yangjiang region. The synoptic classification was based on the spatial distribution of geopotential height at a particular level through the PCA-T analysis. Considering the coastal orography directly interacts with lower-troposphere flows, we finally examined the spatial patterns of 925-hPa geopotential heights over South China (105–121°E, 16–28°N). In this way, the classification tends to result in realistic and physically interpretable flow regimes. Six principal components (PCs) were selected because the differences between neighboring eigenvalues were small since the seventh PC. After significance testing using North's Rule (North et al. 1982), the 6 PCs were retained for classifying the synoptic patterns (namely from Type 1 to Type 6). The integrated explained variance of the 6 PCs accounts for 81.36%. In particular, the explained variance of the Type 1 pattern reaches 28%.

Figure 4 presents the composite geopotential heights and horizontal winds at 925 hPa for each classified synoptic pattern. A total of 62% of the CI days are contributed by two synoptic patterns which are characterized by prevailing low-level southwesterlies over the South China Sea (Figures 4a,b). The most prominent synoptic pattern Type 1 accounts for nearly half of the CI days with the low-level southwesterlies covering almost the entire South China. Such an atmospheric condition primarily occurs in June and July (Table 1) when the southwesterly monsoon is most active. In contrast to Type 1, Type 2 features low-level southwesterlies primarily at sea and mainly occurs in the early stage of summer monsoon from May to June. It is characterized by a low-pressure cyclonic vortex to the west of the region of interest, leading to an evident wind shift supporting the low-level convergence over there (Figure 4b). The other 4 synoptic types account for much less CI days than Types 1 and 2, and are not characterized by southwesterly onshore flows in coastal regions of South China. They appear to be a synoptic pattern in association with monsoon troughs (Figure 4c), tropical disturbances such as tropical cyclones (Figures 4d,f), and the retreat of summer monsoon (Figure 4e). These results suggest the dominance of low-level onshore southwesterlies on CI days, indicative of the important influence of southwesterly monsoon on the convection triggering in coastal areas with orography.

To investigate the lower-troposphere lifting and moisture pooling that are vital to CI under different synoptic circulations, we calculated the vertically integrated moisture flux convergence (VIMFC; Banacos & Schultz, 2005). It was defined as the horizontal moisture flux convergence integrated from 1000 hPa to 850 hPa in the current study. VIMFC combines the influence of horizontal convergence and moisture pooling in a certain depth. Figure 5 shows that a remarked magnitude of low-level moisture flux convergence (negative VIMFC) dominates the coasts of South China including the Yangjiang coastal area under the first two types of atmospheric circulations. It suggests that the onshore southwesterlies at low levels may aid in the large-scale moisture pooling and forced lifting. For the other four types of CI days, a

moisture divergence is generally observed over the coasts (warm colors in Figures 5c–f). Note that convection also initiated under these four synoptic conditions without large-scale moisture pooling, but the probability seems much lower than that under the first two types. Considering that Type 1 accounts for nearly 50% of all the CI days, we focus on the CI-related characteristics under this typical atmospheric circulation in the following sections.

In South China, strong large-scale monsoon flows are often characterized by the presence of marine LLJs. Many high-impact convective weather has been found to occur in the presence of marine LLJs in the coastal region (e.g., Du & Chen, 2018, 2019b; Zhang and Meng, 2019). The marine LLJ is an important factor in influencing the coastal rainfall primarily by providing moisture and convergence at their termini and interacting with orography. For the Type 1 CI days, the occurrence frequency of the upstream marine LLJ is as high as 40%, as indicated by the blue ellipse in Figure 6a. The average wind profile in the high-occurrence LLJ area presents a salient "jet nose" feature (i.e., the speed maximum level) in the lowest 1 km layer (Figure 6b). Due to the averaging for all the Type 1 CI days, the speed on the maximum level of the profile (6.7 m s^{-1}) is smaller than the threshold of 10 m s^{-1} for defining an LLJ. Here such low-level upstream southerlies are defined as the LLJ-like onshore flows. The composite fields of the Type 1 synoptic pattern show that two distinct maxima in wind speed at low levels appear over the sea surface to the west and east of Hainan Island (Figure 7a). The eastern marine LLJ-like southerlies leads to the enhanced coastal convergence below 900 hPa (Figures 7c,d). In higher layers (900–700 hPa), the land region is characterized by strong southwesterlies (Figures 7a,d) which tend to induce the midlevel divergence over the Yangjiang region (Figure 7b). The boundary-layer low-level convergence overlapping with the midlevel divergence, similar to the concept of double LLJ (Du & Chen, 2019a), may jointly strengthen the forced lifting for triggering coastal convection.

4. Impacts of coastal small orography on the detailed spatial pattern of CI

The above analyses suggest that the dominant synoptic pattern (Type 1) generally supports the low-level convergence and moisture pooling on large scales. The detailed CI pattern and convective upscale growth on local scales may be determined by the effects of local orography through disturbing the prevailing low-level ambient airflow. In this section, convection-permitting simulations were conducted to investigate how small-scale orography disturbs the ambient flow and thus determines the detailed spatial patterns of CI in the Yangjiang area.

a. Model configurations and experiment design

The numerical simulations were performed using the fully compressible, nonhydrostatic WRF-ARW Model (Skamarock et al., 2008), version 3.9.1. The domain was designed with a horizontal grid spacing of 3 km (Figure 1a). The peak altitudes of the mountains M2 and M3 in this model configuration are 884 m and 400 m, respectively (Figure 1c). In the vertical, 50 stretched-grid levels with a nominal model top at 50 hPa were used. The main physical parameterization schemes include the WRF single moment six-class (WSM6) microphysics (Hong et al., 2004), the Yonsei State University (YSU) PBL scheme (Noh et al., 2003), and the rapid radiative transfer model (RRTM) for longwave and shortwave radiation schemes (Chou & Suarez, 1994). The cumulus parameterization scheme was not applied because that the cumulus convection can be explicitly represented in the model with the grid spacing of 3 km. Additional sensitive simulations were also conducted in which the coastal orography was artificially removed. In such simulations, the terrain heights were modified in the geographical file named "geo_em.d01.nc" in the WRF Preprocessing System (WPS). The model variables were then directly interpolated to the updated terrain-following coordinates using the ERA5 reanalysis data on pressure level.

The initial and lateral boundary conditions were derived from the averaged pressure-level data of the ERA5 reanalysis for the Type 1 CI days at 0000, 0600, 1200,

and 1800 UTC, respectively. Specifically, the atmospheric fields for the CI days were averaged into a one-day atmosphere (or called "composite atmosphere") at the aforementioned time intervals. Driven by such a composite atmosphere, a 10-day simulation was conducted being initialized at 0000 UTC on 15 May 2017. The lateral boundary conditions (LBCs) were updated every 6 h and the LBCs for the following 9 days were cycled periodically (i.e., duplications of the LBCs at 0000, 0600, 1200, and 1800 UTC on day 1). By such composite simulations, transient atmospheric perturbations tend to be filtered out and the thermally-driven diurnal activity still repeatedly develops (Trier et al., 2010; Bao & Zhang, 2013; Zhang et al., 2014; Chen et al., 2017).

b. Convection in numerical simulations

Figure 8 presents the maximum reflectivity in the morning from day 1 to day 10 obtained from the designed quasi-idealized simulation (hereinafter referred to as the CTL experiment). Driven by the daily cycled LBCs, the simulated results on each day tend to be analogous. Convective cells (maximum reflectivity greater than 40 dBZ) repeatedly initiate to the northeast of the M2 ridge (refer to the cells C1 and C2), on the southern (windward) slopes of M2 (refer to the cell C3), and over the flat terrain surrounded by the four mountains (refer to the cell C4). The convection C4 actually can be tracked to the small-scale mountain M3 (Figures 8j,k). Its early-stage echoes first occur on the southern (windward) slopes of M3. The convection over the major mountain M1 tends to initiate in the early afternoon (refer to the cell C5 in Figure 8*l*). The spatial distribution of these convective cells exhibits a fairly good agreement with the CI hotspots revealed by the long-term radar-based statistics (Figure 3b). Figure 9 presents an example of the radar-observed convective cells in a typical day when the low-level southwesterly winds prevail. The convective cells (refer to the arrows in Figure 9c) were triggered near the small-scale coastal mountains M2 and M3, which are consistent with the simulated ones as shown in Figure 8. It is thus reasonable to

further investigate the role of small-scale orography in producing such a detailed CI pattern with the aid of convection-permitting simulations.

c. Roles of small-scale mountains on CI

The low-level atmosphere in the upstream of the Yangjiang region is characterized by southwesterly onshore flows, leading to that the mountain M2 more or less blocks the moisture flux into the southern slopes of the major mountain M1 (Figure 10a). An additional sensitive experiment by artificially removing the coastal small-scale orography (refer to the dashed polygon region in Figure 1c) was conducted (hereinafter referred to as the NO_TER experiment). In the absence of the upstream small-scale mountains, more moisture is transported to the southern sides of the mountain M1 (Figure 10b). With more water vapor supply, the convective available potential energy (CAPE) remarkedly increases on the windward slopes of the mountain M1 (Figure 10c). The enhanced moisture pooling in the NO_TER experiment leads to that the convection is primarily triggered on the windward slopes of M1 and grows upscale rapidly over there (Figure 11). Consequently, to some extent the existence of the small-scale mountain M2 may have impeded the convective development on the southern slopes of the major mountain M1 by decreasing the low-level moisture transport. The mountain M3 appears to have no significant moisture blocking effect due to its smaller scale than the mountain M2.

In the CTL experiment, the air upstream of the mountains M2 and M3 is generally moist in the lowest 500 m layer (Figure 12; the sounding locations are denoted by the triangles in Figure 10c). The environmental sounding on coastal land is characterized by a high conditional instability. For example, in the early morning before the CI on day 10, the surface-based CAPE and convective inhibition (CIN) values are 2146 J kg^{-1} and 1.4 J kg^{-1}, respectively (Figure 12a). To estimate the dominance of mechanical forcing caused by the interaction between the low-level onshore flow and coastal topography, the Froude number ($Fr = U/NH$, where U is the upstream flow speed, N is the Brunt–Väisälä frequency, and H is the effective mountain height) was calculated

using the offshore sounding (Figure 12b) where airflow tends to be stably stratified. Figure 12c shows that the upstream vertical wind profile is characterized by the maximum oncoming wind speed near the top of the boundary layer at sea (~0.5 km altitude). The average *Fr* values obtained from the levels below the peak heights of M2 and M3 are 1.42 and 2.9, respectively, suggesting the supercritical ($Fr > 1$) oncoming flow that the air tends to pass over the mountains of interest (e.g., Smith 1979; Hagen et al. 2011).

Figure 13 shows that the upslope flows converge over the windward slopes of M2 and M3 with the forced upward motions extending hundreds of meters higher than the level of free convection (LFC). Although the updrafts are weak, shallow convection tends to easily initiate because the lifting is relatively persistent, as shown by the convective cells C3 and C4 (Figure 8). Specifically, on the windward slopes of M2, the near-surface air is nearly saturated and is characterized by very low lifting condensation level (LCL) and LFC (Figure 13a). The calculated CIN value at the location denoted by the yellow dot in Figure 13a is nearly 0 J kg^{-1} at 0800 LST. Without any convective inhibition, the moist airmasses tend to be easily lifted above their LFC even with small forced lifting. Figure 8k shows that shallow convection appears near the windward ridge of M2 because the forced updrafts are relatively weak and shallow. This shallow convection rapidly grows upscale to deep convection as it propagates over the downwind sides of the mountains.

When the supercritical oncoming flow passes over the mountain ridges, the mountain wave behavior is observed on the downwind slopes (Figure 13; Durran, 1986; Doyle & Durran, 2002). A region of positive buoyancy downstream of the ridge forms due to the depressed isentropes in the wake of obstacle, leading to the formation of updraft branch oriented in the uphill direction. On the downwind slopes of M2, the environmental sounding at the location denoted by the green dot in Figure 13a is characterized by a CIN value of 0.25 J kg^{-1}. According to the simple estimate from the parcel theory, a strength of upward motion ($\sqrt{2 * \mathrm{CIN}}$) of approximately 0.7 m s^{-1} is

required to overcome the inhibition to the LFC. Figure 13a shows that the updraft strength is not strong enough at 0800 LST, though the updraft branch extends to an altitude of 2.5 km. When the boundary layer is destabilized due to the diurnal heating in the daytime (corresponding to the decreasing Brunt–Väisälä frequency), the mountain wave induced updrafts may be intensified to overcome the CIN (e.g., Figure 14) and thus initiate convection on the downwind slopes (Figure 8). In addition, the diurnal heating may also promote the lifting for CI by the enhanced thermal-driven circulation due to the differential heating between mountains and surrounding plains. On the other hand, the diurnal heating tends to dry the near-surface air and moisten the upper part of PBL through the vertical mixing from the early morning to afternoon (Figure 14). The daytime CI occurs when the forced lifting gradually intensifies while the near-surface moisture decreases, suggesting the dominance of lifting in the CI process.

It is worth noting that lee-side mountain waves also exist after sunset while convection barely initiates on the downwind slopes at night. For instance, Figure 14a shows that the upward motions with a magnitude greater than 0.1 m s^{-1} are located on the downwind slopes of the mountain M2 at 0400 LST when no convection occurs. These wave-induced lee-side updrafts are elevated relative to the mountain foot while the moist layer is relatively shallow due to the suppressed turbulent mixing in the nighttime (refer to the height of the low-level moist layer in Figure 14a). The elevated wave-induced updrafts generally locating above the near-surface moist layer tend to result in the nocturnal CI failure in that region. As the moist layer deepens in the daytime, the airmasses lifted by the lee-side updrafts are characterized by greater moist static energy and thus are more easily to reach the LFC, achieving and maintaining positive buoyancy (Figure 14b). Additionally, the upward motions over the mountains also tend to be enhanced by thermals during the day. The spatial collocation between the deepening moist boundary layer and the lee-side upward motions is one of the key factors to initiate the lee-side convection. In the simulations, the lee-wave-induced

convection tends to maintain when it propagates over the enhanced horizontal convergence zone that is caused by the low-level flows pass around the mountains.

Because the mountains M2 and M3 are relatively isolated at a small horizontal scale, the low-level onshore flows also freely pass around these two obstacles leading to the baroclinic vorticity generation (Smolarkiewicz & Rotunno, 1989). A pair of counter-rotating vortices occur in the wake region with the positive vertical vorticity located on the downwind right of the orography (Figure 15a). Enhanced convergence zones extend from the lee sides of these two small-scale mountains to the flat region where the observed CI hotspot is located (labeled P1 and P2 in Figures 15b,c). In some cases, convection is directly triggered over these lee-side convergence zones with positive vertical vorticity (e.g., the convective cells C1 and C2 in Figure 8). The strength of horizontal convergence downwind of the mountain M3 is weaker than that of the larger mountain M2. Nevertheless, this lee-side convergence also supports the upscale growth of the convection that originates from the upwind slope of M3 (e.g., the cell C4 in Figures 8j,k). Figure 13b shows that the low-level upward motions are significantly enhanced when the convective cell C4 propagates to the lee sides of M3.

5. Summary

A 7-yr climatology of warm-season convection triggering at a hotspot of coastal rainfall in South China is presented. The CI occurrences identified using radar observations are primarily associated with isolated storms. In the region of interest (around Yangjiang city in Guangdong Province), two small-scale coastal mountains (M2 and M3) are located to the south of a larger-scale mountain (M1). The local maxima in CI occurrence are located over the flat terrain downwind of the small-scale mountains rather than on the windward slopes of the major mountain M1. The statistics show that the genesis of convection in the Yangjiang area exhibits an evident diurnal variation. Nearly 64% CI occurrences appear in the daytime and are concentrated on coastal land. By contrast, the nocturnal CI mainly takes place on coastlines and in

offshore areas. The formation process for the daytime CI associated with these small-scale coastal mountains are summarized in the schematic diagram in Figure 16 and the conclusions below.

The lower troposphere on CI days is dominated by southwesterlies with a high occurrence frequency of marine LLJs, aiding in the low-level moistening in the coastal area. This atmospheric condition is common in the southwesterly monsoon season, suggesting the important role of onshore monsoonal flows in supporting the genesis of coastal convection. The Yangjiang area tends to undergo an environmental preconditioning to CI through the marine moisture transport and large-scale mean ascent caused by the deceleration of the LLJ-like onshore flow from the South China Sea. On local scales, the detailed spatial patterns of CI revealed by the radar-based statistics were demonstrated to owe to small-scale orographic disturbances that lead to local variations in moisture pooling and dynamic lifting.

Driven by the atmospheric conditions of the dominant synoptic pattern on CI days, quasi-idealized convection-permitting simulations were conducted to investigate the impacts of small-scale coastal orography on the detailed spatial pattern of CI occurrence. The simulated convection exhibits a fairly good agreement with radar observations in regards to reproducing the convection that repeatedly occurs in the observed CI regions. Convection frequently initiates on the downwind slopes and over the flat terrain to the northeast of the small-scale coastal mountains (M2 and M3). Under this synoptic pattern that is characterized by the LLJ-like southerly marine flow at low levels, the coastal mountains are dominated the supercritical oncoming flow (Froude number greater than 1), which leads to the mechanical lifting on the windward slopes and mountain waves on the downwind slopes of the mountains. In addition to such mechanical forcings, the lee-side convergence with positive vertical vorticity also supports the genesis of convection downwind of the mountains when the onshore flow passes around these isolated obstacles. In the thermodynamic perspective, the presence of upstream coastal orography (primarily the mountain M2) decreases the low-level

moisture pooling on the southern slopes of the major mountain M1, which to some extent impedes the convective development over the major mountain. When the small-scale mountains were artificially removed, convection would form on the windward sides of the major mountain and undergo a more vigorous convective growth.

The findings suggest that the disturbance of small-scale orography on the lower-troposphere ambient flow can generate substantial local variations in dynamic lifting and moisture pooling, which may be vitally important in determining the location that CI repeatedly occurs on local scales. An explicit resolving of such local orography-induced flow modification is warranted to improve the severe weather modeling on monsoon coasts. Regarding the importance of onshore monsoonal flows in the triggering of coastal convection, an improved modeling of their strengths and prevailing directions is also an indispensable part. More atmospheric observations at sea regarding the horizontal heterogeneity and vertical structure of the low-level onshore flow are needed to better depict the ambient circulations over coastal regions. The current study primarily focused on the daytime CI in the Yangjiang area. Future investigation efforts would be directed toward the detailed triggering mechanisms of the nocturnal convection.

Acknowledgments

This study was funded by the National Natural Science Foundation of China (41905043, 41775094, 41905049, 42030604), and the Key Technology Development Project for Meteorological Operational Forecast of CMA (YBGJXM(2020)3A-01). The CMORPH data provided by NOAA (https://www.cpc.ncep.noaa.gov/products/janowiak/cmorph_description.html) and the ERA5 reanalysis data provided by ECMWF (https://cds.climate.copernicus.eu/cdsapp#!/dataset/reanalysis-era5-pressure-levels?tab=form) are gratefully acknowledged. The numerical simulations were performed on TianHe-1 (A) at National Supercomputer Center in Tianjin, China.

References

American Meteorological Society, accessed on 6 August 2021 at https://glossary.ametsoc.org/wiki/Moisture_pooling

Bai, L., Chen, G., & Huang, L. (2020a). Convection initiation in monsoon coastal areas (South China). *Geophysical Research Letters*, 47, e2020GL087035. https://doi.org/10.1029/2020GL087035

Bai, L., Chen, G., & Huang, L. (2020b). Image processing of radar mosaics for the climatology of convection initiation in South China. *Journal of Applied Meteorology and Climatology*, 59, 65–81, https://doi.org/10.1175/JAMC-D-19-0081.1

Banacos, P. C., & Schultz, D. M. (2005). The use of moisture flux convergence in forecasting convective initiation: historical and operational perspectives. *Weather and Forecasting*, 20, 351–366.

Bao, X., & Zhang, F. (2013). Impacts of the mountain–plains solenoid and cold pool dynamics on the diurnal variation of warm-season precipitation over northern China. *Atmospheric Chemistry and Physics*, 13, 6965–6982, https://doi.org/10.5194/acp-13-6965-2013

Bao, X., Luo, Y., & Gao, X. (2021). The synoptic impacts on the convection initiation of a warm-sector heavy rainfall event over coastal South China prior to the monsoon onset: A numerical modeling study. *Journal of Geophysical Research: Atmospheres*, 126, e2020JD034335. https://doi.org/10.1029/2020JD034335

Banta, R. M., & Barker Schaaf, C. (1987). Thunderstorm genesis zones in the Colorado Rocky Mountains as determined by traceback of geosynchronous satellite images. *Monthly Weather Review*, 115, 463–476, https://doi.org/10.1175/1520-0493(1987)115<0463:TGZITC>2.0.CO;2

Chen, G., Lan, R., Zeng, W., Pan, H., & Li, W. (2018). Diurnal variations of rainfall in surface and satellite observations at the monsoon coast (South China). *Journal of Climate*, 31, 1703–1724, https://doi.org/10.1175/JCLI-D-17-0373.1

Chou, M.-D., & Suarez, M. J. (1994). An efficient thermal infrared radiation parameterization for use in general circulation models. NASA Technical Memorandum, NASA, 84 pp.

Chen, X., Zhao, K., & Xue, M. (2014). Spatial and temporal characteristics of warm season convection over Pearl River Delta region, China, based on 3years of operational radar data. *Journal of Geophysical Research: Atmospheres*, 119, 12447–12465.

Chen, X., Zhang, F., & Zhao, K. (2016). Diurnal variations of the land–sea breeze and its related precipitation over South China. *Journal of the Atmospheric Sciences*, 73, 4793–4815, https://doi.org/10.1175/JAS-D-16-0106.1

Chen, X., Zhang, F., & Zhao, K. (2017). Influence of monsoonal wind speed and moisture content on intensity and diurnal variations of the Mei-Yu season coastal rainfall over South China, *Journal of the Atmospheric Sciences.* 74, 2835–2856, https://doi.org/10.1175/JAS-D-17-0081.1

Doyle, J. D., and D. R. Durran, 2002: The dynamics of mountain-wave-induced rotors, *Journal of the Atmospheric Sciences*, 59, 186–201, https://doi.org/10.1175/1520-0469(2002)059<0186:TDOMWI>2.0.CO;2

Du, Y., & Chen, G. (2019a). Heavy rainfall associated with double low-level jets over southern China. Part II: convection initiation. *Monthly Weather Review*, 147, 543–565, https://doi.org/10.1175/MWR-D-18-0102.1.

Du, Y., & Chen, G. (2019b). Climatology of low-level jets and their impact on rainfall over southern China during the early-summer rainy season. *Journal of Climate*, 32, 8813–8833, https://doi.org/10.1175/JCLI-D-19-0306.1

Du, Y., Zhang, Q., Chen, Y., Zhao, Y., & Wang, X. (2014). Numerical simulations of spatial distributions and diurnal variations of low-level jets in China during early summer. *Journal of Climate*, 27, 5747–5767, https://doi.org/10.1175/JCLI-D-13-00571.1

Durran, D.R. (1986). Another look at downslope windstorms. Part I: On the development of analogs to supercritical flow in an infinitely deep continuously stratified fluid. *Journal of the Atmospheric Sciences*, 93, 2527–2543, https://doi.org/10.1175/1520-0469(1986)043<2527:ALADWP>2.0.CO;2

Gebauer, J. G., Shapiro, A., Fedorovich, E., & Klein, P. (2018). Convection initiation caused by heterogeneous low-level jets over the Great Plains. *Monthly Weather Review*, 146, 2615–2637, https://doi.org/10.1175/MWR-D-18-0002.1

Geerts, B., & Coauthors. (2017). The 2015 Plains Elevated Convection at Night field project. *Bulletin of the American Meteorological Society*, 98, 767–786, https://doi.org/10.1175/BAMS-D-15-00257.1.

Hagen, M., Baelen, J. van & Richard, E. (2011). Influence of the wind profile on the initiation of convection in mountainous terrain. *Quarterly Journal of the Royal Meteorological Society*, 137, 224–235, https://doi.org/10.1002/qj.784

Hersbach, H., & Coauthors. (2020). The ERA5 global reanalysis. *Quarterly Journal of the Royal Meteorological Society*, 146, 1999–2049, https://doi.org/10.1002/qj.3803

Hong, S.-Y., Dudhia, J., & Chen, S.-H. (2004). A revised approach to ice microphysical processes for the parameterization of clouds and precipitation. *Monthly Weather Review*, 132, 103–120, https://doi.org/10.1175/1520-0493(2004)132<0103:ARATIM>2.0.CO;2

Huffman, G. J., Bolvin, D. T., Nelkin, E. J., Wolff, D. B., Adler, R. F., Gu, G., Hong, Y., Bowman, K. P., & Stocker, E. F. (2007). The TRMM Multisatellite Precipitation Analysis (TMPA): Quasi-global, multiyear, combined-sensor precipitation estimates at fine scales, *Journal of Hydrometeorology*, 8, 38–55, https://doi.org/10.1175/JHM560.1

Huth R. (1996). Properties of the circulation classification scheme based on the rotated principal component analysis. *Meteorology and Atmospheric Physics*, 59, 217–233, https://doi.org/10.1007/BF01030145

Huth R. (2000). A circulation classification scheme applicable in GCM studies. *Theoretical and Applied Climatology*, 67, 1–18, https://doi.org/10.1007/s007040070012

Joyce, R. J., Janowiak, J. E., Arkin, P. A., & Xie, P. (2004). CMORPH: A method that produces global precipitation estimates from passive microwave and infrared data at high spatial and temporal resolution. *Journal of Hydrometeorology*, 5, 487–503, https://doi.org/10.1175/1525-7541(2004)005<0487:CAMTPG>2.0.CO;2

Li, J., Li, N., & Yu, R. (2019). Regional differences in hourly precipitation characteristics along the western coast of South China. *Journal of Applied Meteorology and Climatology*, 58, 2717–2732, https://doi.org/10.1175/JAMC-D-19-0150.1

Liu, X., Luo, Y., Huang, L., Zhang, D.-L., & Guan, Z. (2020). Roles of double low-level jets in the generation of coexisting inland and coastal heavy rainfall over South China during the presummer rainy season. Journal of Geophysical Research: Atmospheres, 125, e2020JD032890

Luo, Y., & Coauthors. (2017). The Southern China Monsoon Rainfall Experiment (SCMREX). *Bulletin of the American Meteorological Society*, 98, 999–1013, https://doi.org/10.1175/BAMS-D-15-00235.1

Luo, Y., Xia, R., & Chan, J. C. L. (2020). Characteristics, physical mechanisms, and prediction of pre-summer rainfall over South China: research progress during 2008–2019. *Journal of the Meteorological Society of Japan*, 98, 19−42, https://doi.org/10.2151/jmsj.2020-002

Markowsk, P., & Richardson, Y. (2010). Mesoscale meteorology in midlatitudes. Wiley-Blackwell, 407 pp.

Noh, Y., Cheon, W.-G., Hong, S.-Y., & Raasch, S. (2003). Improvement of the K-profile model for the planetary boundary layer based on large eddy simulation data. *Boundary-Layer Meteorology*, 107, 401–427, https://doi.org/10.1023/A:1022146015946

Philipp, A., Beck, C., Huth, R., & Jacobeit, J. (2016). Development and comparison of circulation type classifications using the COST 733 dataset and software. *International Journal of Climatology*, 36, 2673–2691. https://doi.org/10.1002/joc.3920

Rao, X., Zhao, K., Chen, X., Huang, A., Xue, M., Zhang, Q., & Wang, M. (2019). Influence of synoptic pattern and low-level wind speed on intensity and diurnal variations of orographic convection in summer over Pearl River Delta, South China. *Journal of Geophysical Research: Atmospheres*, 124, 6157–6179, https://doi.org/10.1029/2019JD030384

Reif, D. W., & Bluestein, H. B. (2017). A 20-year climatology of nocturnal convection initiation over the central and southern Great Plains during the warm season. *Monthly Weather Review*, 145, 1615–1639, https://doi.org/10.1175/MWR-D-16-0340.1

Saito, K., Kunii, M., & Araki, K. (2018). Cloud Resolving Simulation of a Local Heavy Rainfall Event on 26 August 2011 Observed in TOMACS. *Journal of the Meteorological Society of Japan*, 96A, 175–199, https://doi.org/10.2151/jmsj.2018-027

Smolarkiewicz, P. K., & Rotunno, R. (1989). Low Froude number flow past three-dimensional obstacles. Part I: Baroclinically Generated Lee Vortices. *Journal of Atmospheric Sciences*, 46, 1154–1164.

Skamarock, W. C., & Coauthors. (2008). A description of the Advanced Research WRF version 3. NCAR Tech. Note, NCAR/TN-4751STR, NCAR/MMM, 113 pp., https://doi.org/10.5065/D68S4MVH

Shapiro, A., Fedorovich, E., & Gebauer, J. G. (2018). Mesoscale ascent in nocturnal low-level jets. *Journal of Atmospheric Sciences*, 75, 1403– 1427, https://doi.org/10.1175/JAS-D-17-0279.1

Schaaf, C. B., Wurman, J., & Banta, R. M. (1988). Thunderstorm-producing terrain features. *Bulletin of the American Meteorological Society*, 69, 272–277, https://doi.org/10.1175/1520-0477(1988)069<0272:TPTF>2.0.CO;2

Smith, R. B., 1979: The influence of mountains on the atmosphere. Advances in Geophysics, Vol. 21, Academic Press, 87–230, https://doi.org/10.1016/S0065-2687(08)60262-9

Trier, S. B., Davis, C. A., & Ahijevych, D. A. (2010). Environmental controls on the simulated diurnal cycle of warm-season precipitation in the continental United

States. *Journal of the Atmospheric Sciences,* 67, 1066–1090, https://doi.org/10.1175/2009JAS3247.1

Trier, S. B., Wilson, J. W., Ahijevych, D. A., & Sobash, R. A. (2017). Mesoscale vertical motions near nocturnal convection initiation in PECAN. *Monthly Weather Review*, 145, 2919–2941, https://doi.org/10.1175/MWR-D-17-0005.1

Wang, C., Zhao, K., Huang, A., Chen, X., & Rao, X. (2021). The crucial role of synoptic pattern in determining the spatial distribution and diurnal cycle of heavy rainfall over the South China coast. *Journal of Climate*, 34, 2441–2458, https://doi.org/10.1175/JCLI-D-20-0274.1

Wilson, J. W., & Roberts, R. D. (2006). Summary of convective storm initiation and evolution during IHOP: Observational and modeling perspective. *Monthly Weather Review*, 134, 23–47, https://doi.org/10.1175/MWR3069.1

Wu, N., Ding, X., Wen, Z., Chen, G., Meng, Z., Lin, L., & Min, J. (2020). Contrasting the frontal and warm-sector heavy rainfalls over South China during the early-summer rainy season. *Atmospheric Research*, 235, 104693, https://doi.org/10.1016/j.atmosres.2019.104693

Xie, S.-P., Xu, H., Saji, N., Wang, Y., & Liu, W. (2006). Role of narrow mountains in large-scale organization of Asian monsoon convection. *Journal of Climate*, 19, 3420–3429, https://doi.org/10.1175/JCLI3777.1

Yu, R., Xu, Y., Zhou, T., & Li, J. (2007). Relation between rainfall duration and diurnal variation in the warm season precipitation over central eastern China, *Geophysical Research Letters*, 34, L13703, https://doi.org/10.1029/2007GL030315

Zhang, M., & Meng, Z. (2018). Impact of synoptic-scale factors on rainfall forecast in different stages of a persistent heavy rainfall event in south China. *Journal of Geophysical Research: Atmospheres*, 123, 3574–3593, https://doi.org/10.1002/2017JD028155

Zhang, M., Meng, Z., Huang, Y., & Wang, D. (2019). The mechanism and predictability of an elevated convection initiation event in a weak-lifting environment in central-eastern China. *Monthly Weather Review*, 147, 1823–1841, https://doi.org/10.1175/MWR-D-18-0400.1

Zhang, Q., Ni, X., & Zhang, F. (2017). Decreasing trend in severe weather occurrence over China during the past 50 years. *Scientific Reports*, 7, 42310, https://doi.org/10.1038/srep42310

Zhang, Y., Sun, J., & Fu, S. (2014). Impacts of diurnal variation of mountain-plain solenoid circulations on precipitation and vortices east of the Tibetan Plateau during the Mei-yu season. *Advances in Atmospheric Sciences*, 31, 139–153, https://doi.org/10.1007/s00376-013-2052-0

Tables

Table 1. The number of the CI days corresponding to the six synoptic types in each month.

	April	May	June	July	August	September
Type 1	14	38	60	54	35	13
Type 2	6	18	25	3	15	9
Type 3	9	7	10	19	9	8
Type 4	1	8	7	8	23	3
Type 5	4	1	0	4	13	25
Type 6	1	1	1	6	5	3

Figures with captions

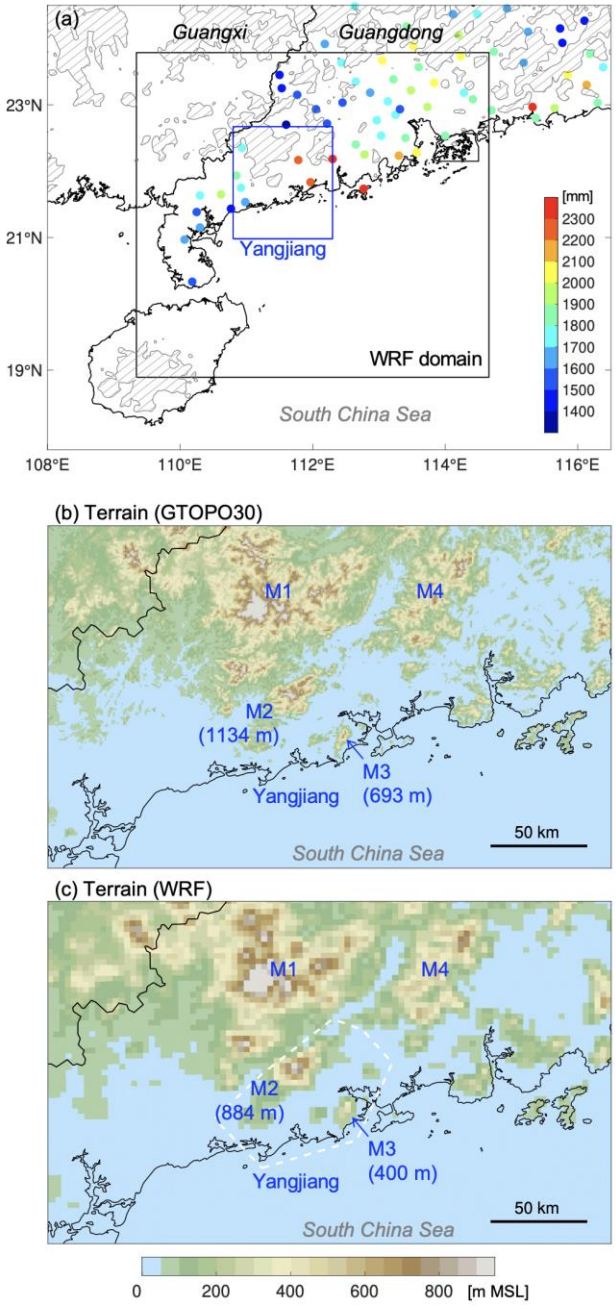

Figure 1. (a) WRF model domain configuration (black rectangle). The colored dots present the annual rainfall accumulation averaged over the period of 2000–2014 obtained from surface gauge stations in Guangdong Province. The blue rectangle represents the Yangjiang region. The hatched area within the contours indicates the terrain at an altitude of above 250 m. (b) Terrain heights plotted using the geographic data GTOPO30 (https://earthexplorer.usgs.gov/). The mountains labeled M1–M4 are described in the text. The peak heights of the mountains M2 and M3 are labeled. (c) Terrain heights in the 3-km WRF simulation. The dashed white polygon outlines the region where the orography is artificially removed in the NO_TER simulation.

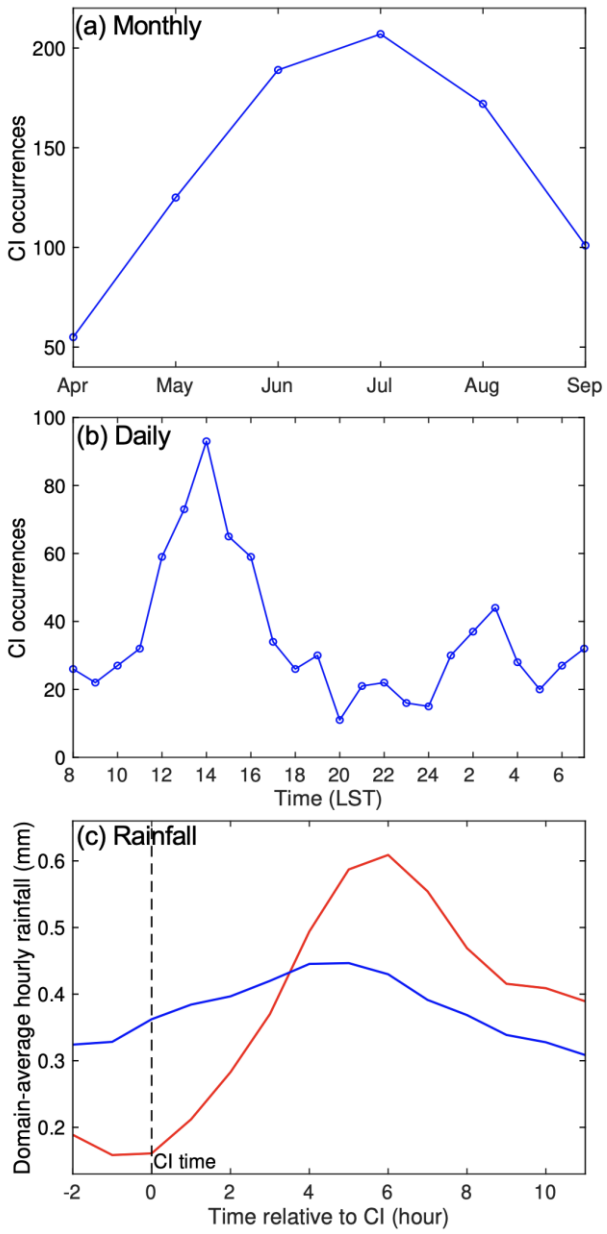

Figure 2. (a) Monthly and (b) diurnal variations of the CI occurrences within the blue box as shown in Figure 1a during April–September from 2013 to 2019. (c) Domain-average hourly CMORPH rainfall (red) before and after the CI time averaged for all CI events. For each CI event, the domain-average hourly rainfall on the particular date in each year from 2013 to 2019 was extracted and then averaged to obtain the climatological mean rainfall (blue curve) in a certain hour relative to CI.

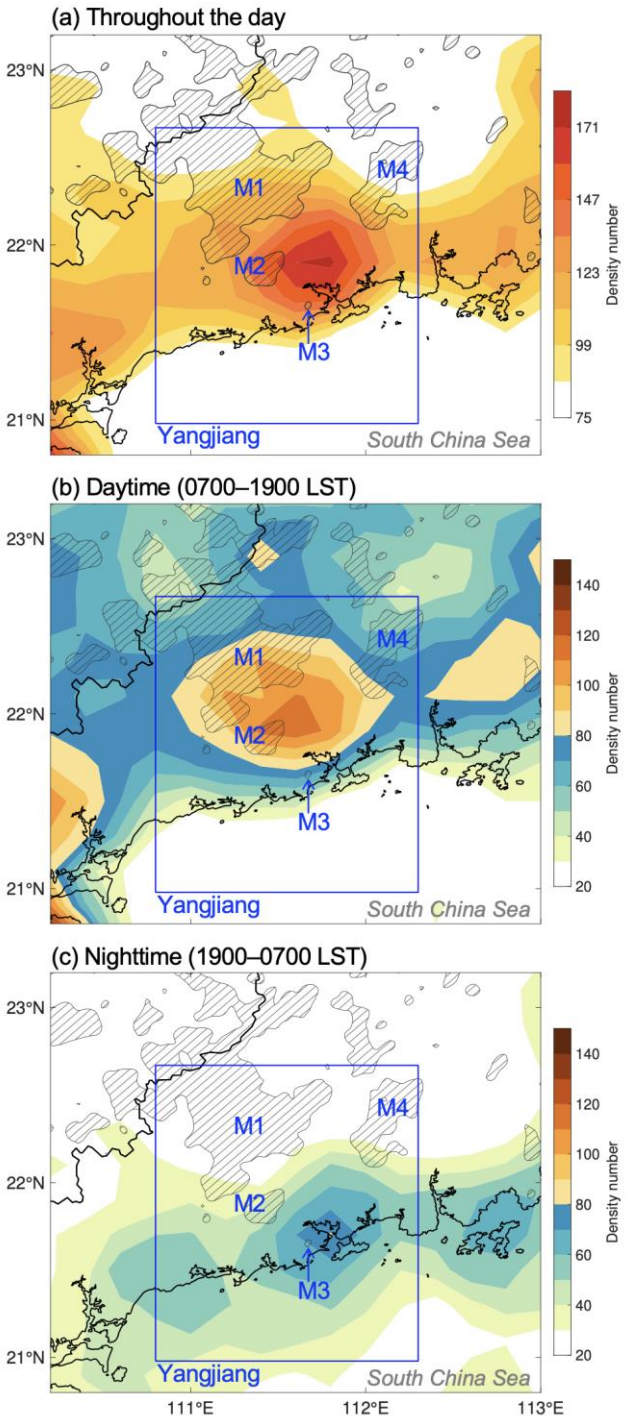

Figure 3. Density number of CI occurrence during April–September from 2013 to 2019. The density number at a grid point is obtained by assigning the count of CI occurrences within 30 km. The hatched area within the contours indicates the terrain at an altitude of above 250 m. The mountains labeled M1, M2, M3 and M4 within the study region (blue box) are described in the text.

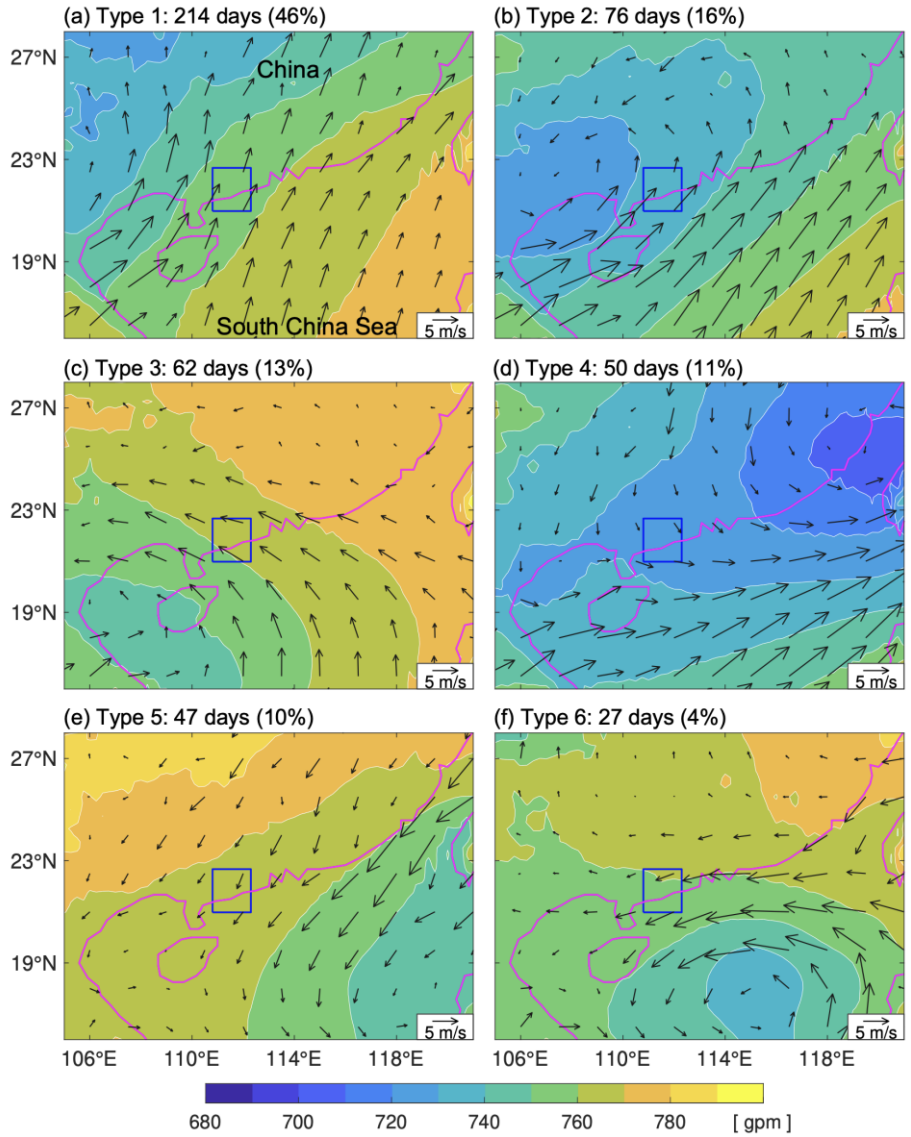

Figure 4. The six synoptic patterns (types 1–6) based on geopotential height at 925 hPa (shading) in South China at 1100 LST averaged on CI days during April–September from 2013 to 2019. The number of days for each pattern and their percentages are shown in the subtitles. The mean horizontal wind vectors at 925 hPa are also superimposed. The blue box represents the Yangjiang region.

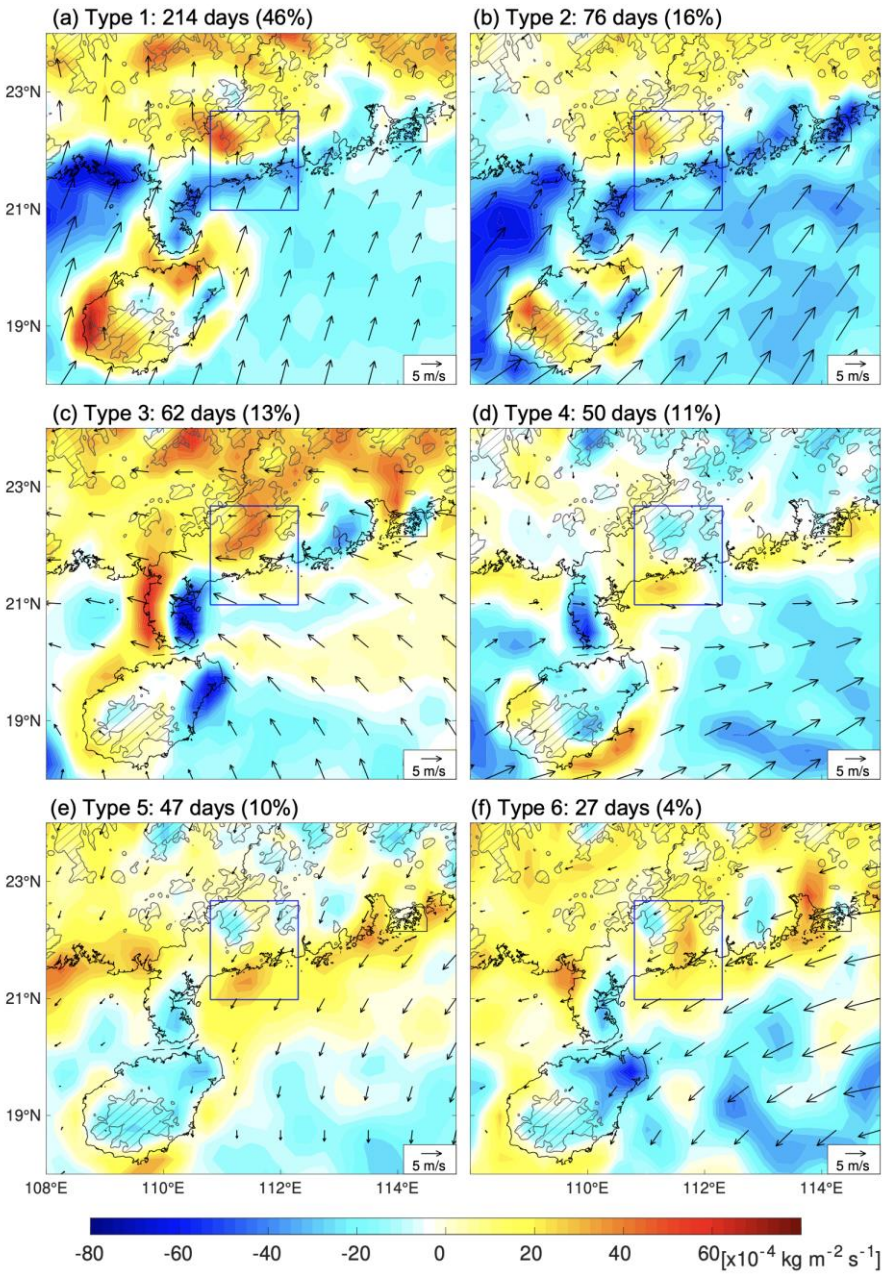

Figure 5. Composites of the vertically integrated moisture flux convergence (VIMFC; shading) at 1100 LST for the six synoptic patterns (Figure 4), respectively. A composite is obtained by averaging the VIMFC on each CI day for the same synoptic type. The negative values indicate the convergence effect. The mean horizontal wind vectors at 950 hPa are also superimposed. The blue box represents the Yangjiang region. The hatched area within the contours indicates the terrain at an altitude of above 250 m.

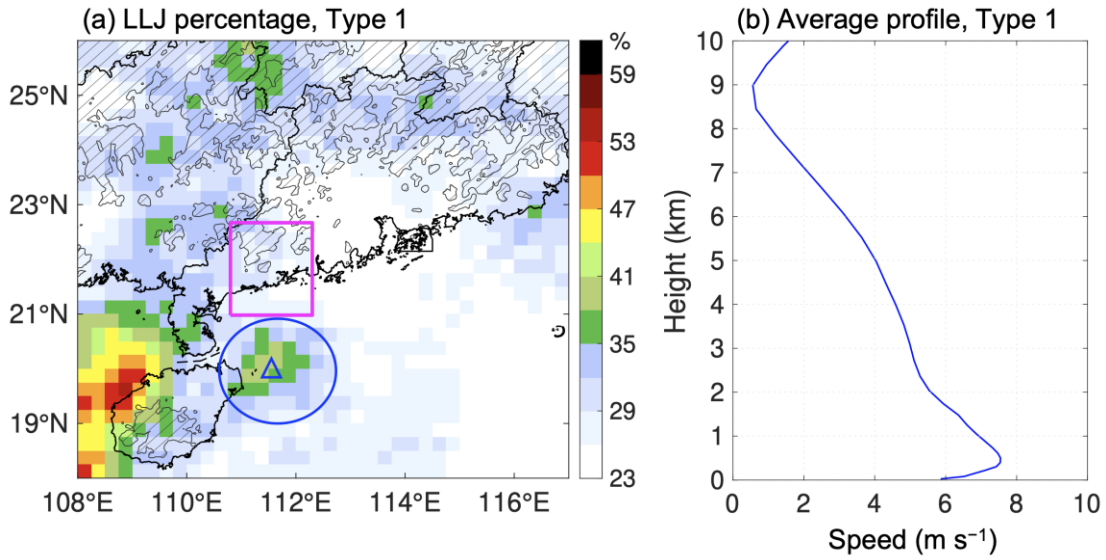

Figure 6. (a) The percentage of LLJ occurrence on the CI days for the synoptic type 1. The magenta box represents the Yangjiang region. The hatched area within the contours indicates the terrain at an altitude of above 250 m. (b) The average vertical wind profile at the location denoted by the blue triangle in (a).

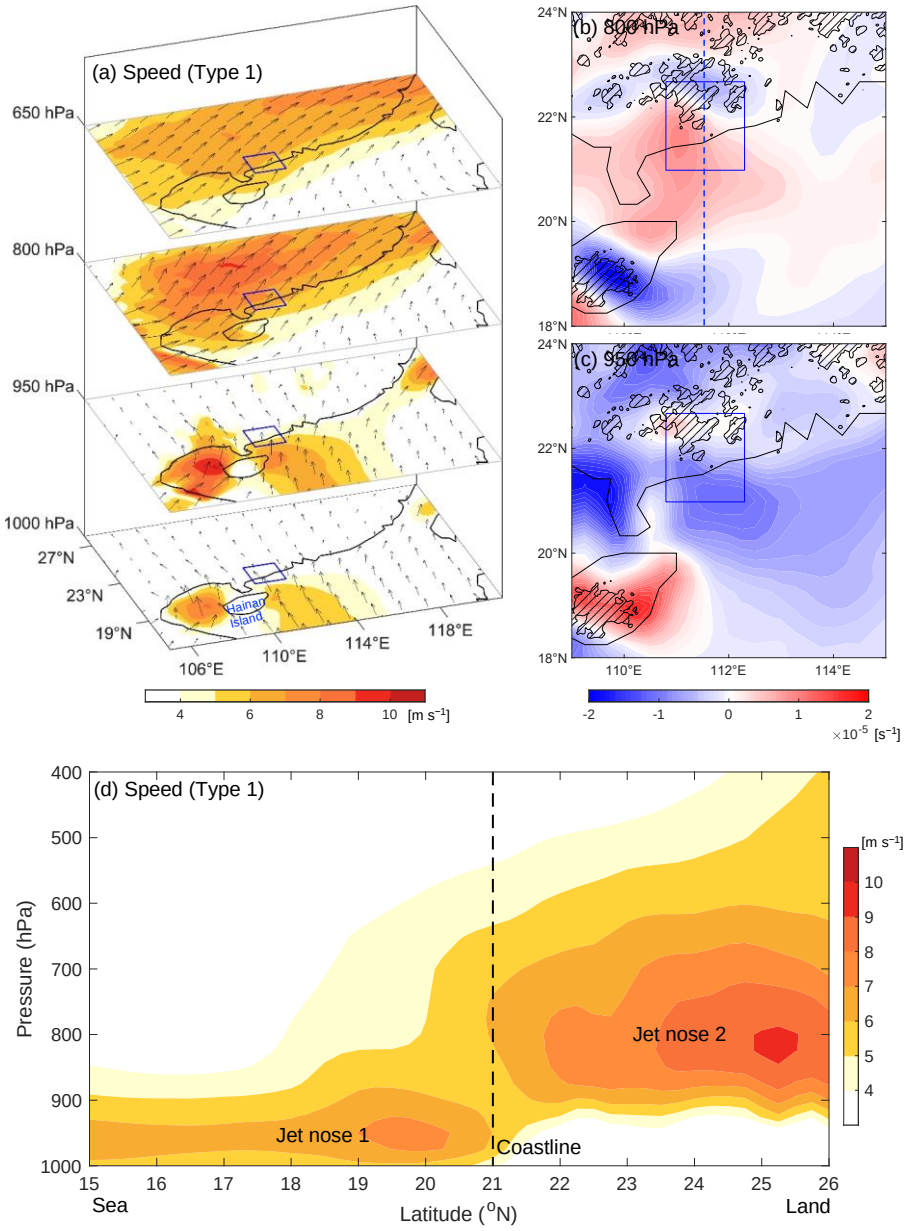

Figure 7. (a) Speeds (shading) of the horizontal winds (vectors) on different levels averaged on the CI days for the Type 1 synoptic pattern. Convergence (cool color) and divergence (warm color) on (b) 800 hPa and (c) 950 hPa are also given for reference. The hatched area within the contours indicates the terrain at an altitude of 250 m. The blue box represents the Yangjiang region. (d) Vertical cross section of wind speed along the dashed line in (b).

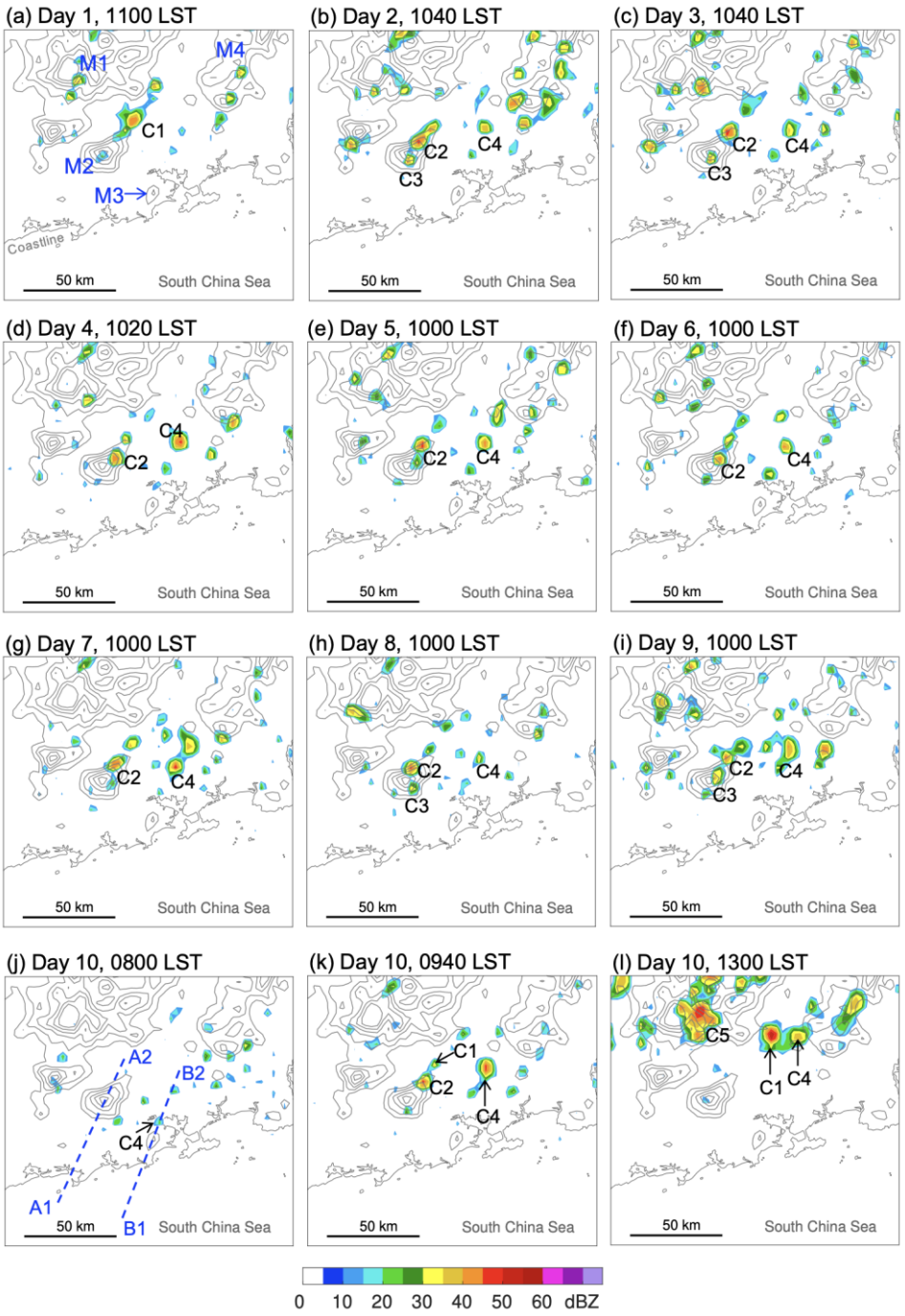

Figure 8. Maximum reflectivity at each vertical column obtained from the CTL experiment. The terrain heights from 200 m to 950 m are contoured with an interval of 100 m. The major mountains labeled M1, M2 and M3 and the convective cells C1, C2, and C3 are described in the text. In (j), the dashed lines A1–A2 and B1–B2 indicate the locations for the vertical cross sections as shown in Figures 13 and 14.

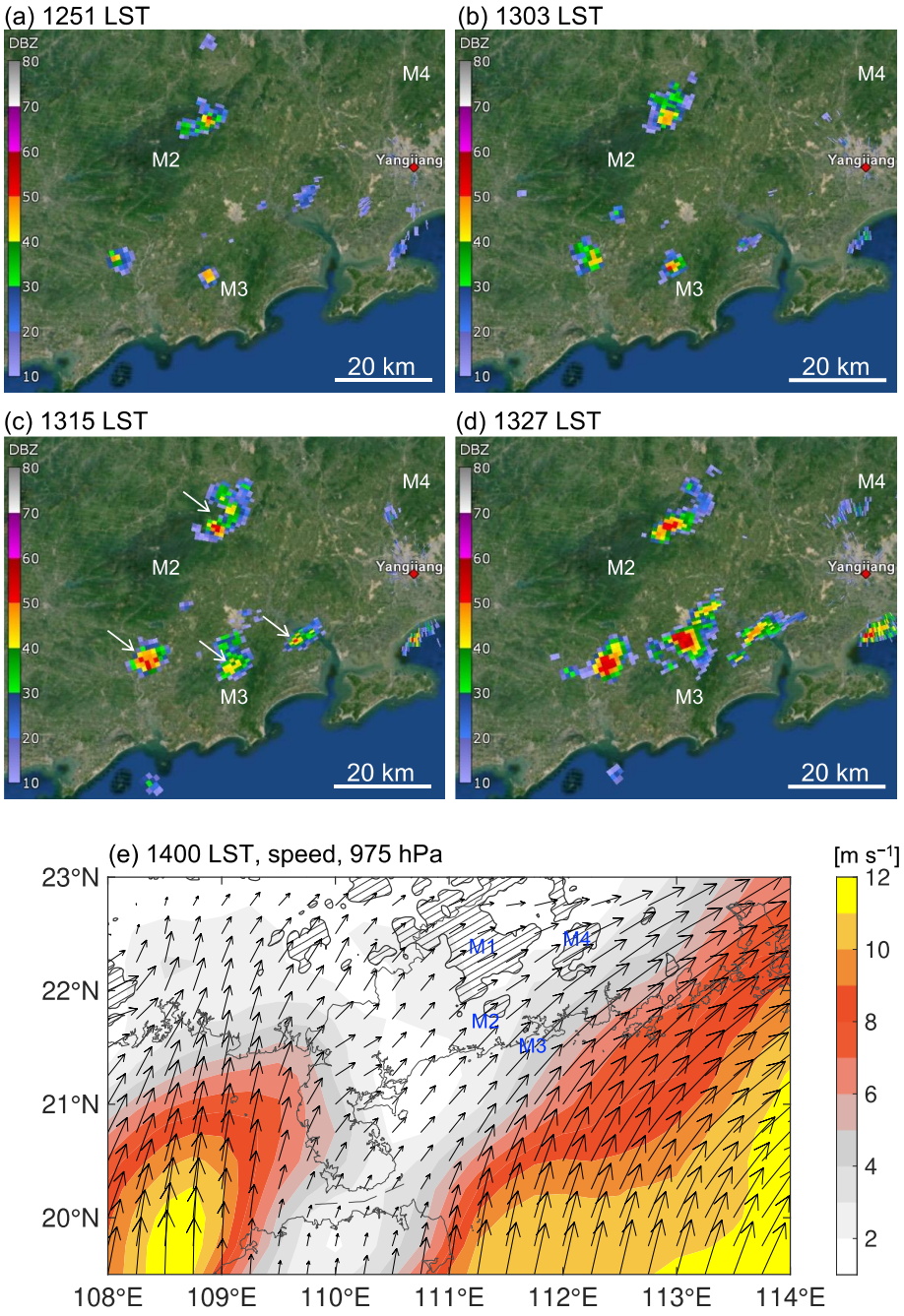

Figure 9. Reflectivity (units: dBZ) at the 4.3° elevation angle from the Yangjiang operational radar (S-band; red diamond) at (a) 1251, (b) 1303, (c) 1315 and (d) 1327 LST on 13 June 2017. The convective cells discussed in the text are denoted by the arrows in (c). (d) Speed of the horizontal winds (vectors) on 975 hPa calculated from the ERA5 reanalysis data. The hatched area within the contours indicates the terrain at an altitude of above 250 m.

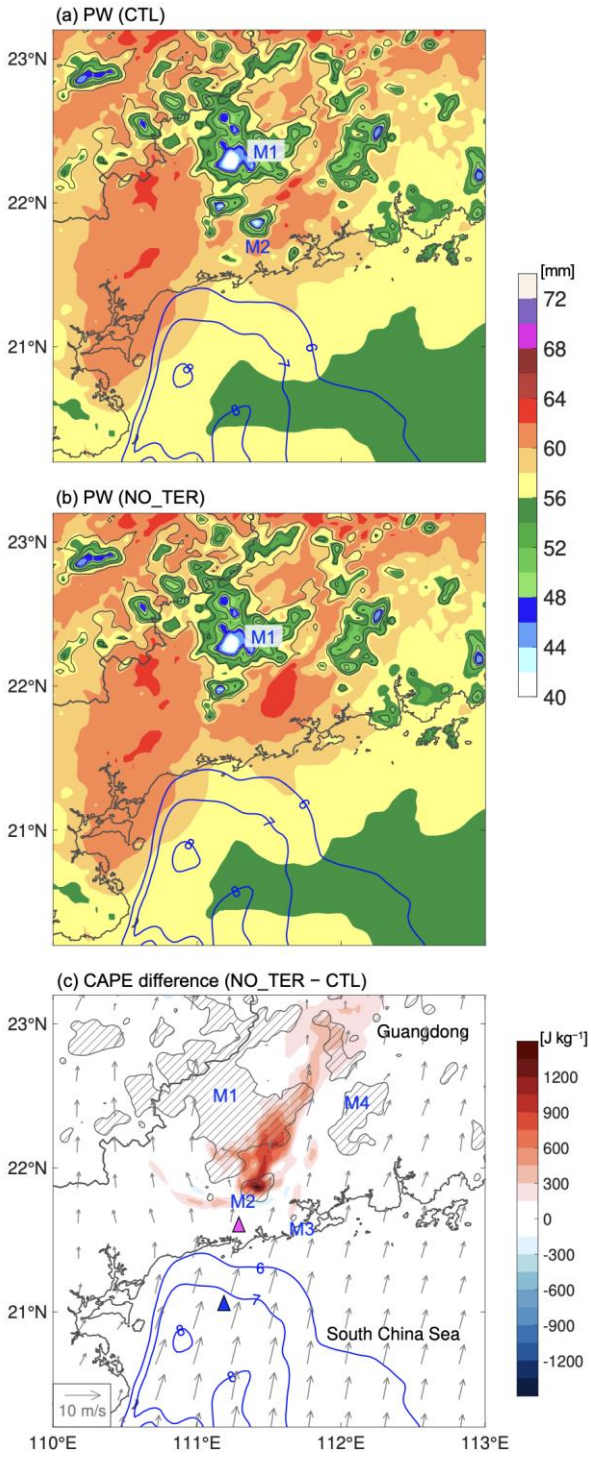

Figure 10. Precipitable water (PW) for the (a) CTL and (b) NO_TER experiments at 0800 LST on day 10. The terrain heights from 200 m to 950 m are contoured with an interval of 100 m. (c) Difference of the surface-based CAPE between the NO_TER and CTL experiments. Horizontal winds (vectors) at 400 m altitude in the CTL experiment are shown for reference. The speed of the wind over South China Sea is contoured from 6 m s^{-1}. The hatched area within the contours indicates the terrain at an altitude of above 250 m. The magenta and blue triangles in (c) denote the locations of the skew *T*–log *p* diagrams given in Figure 12.

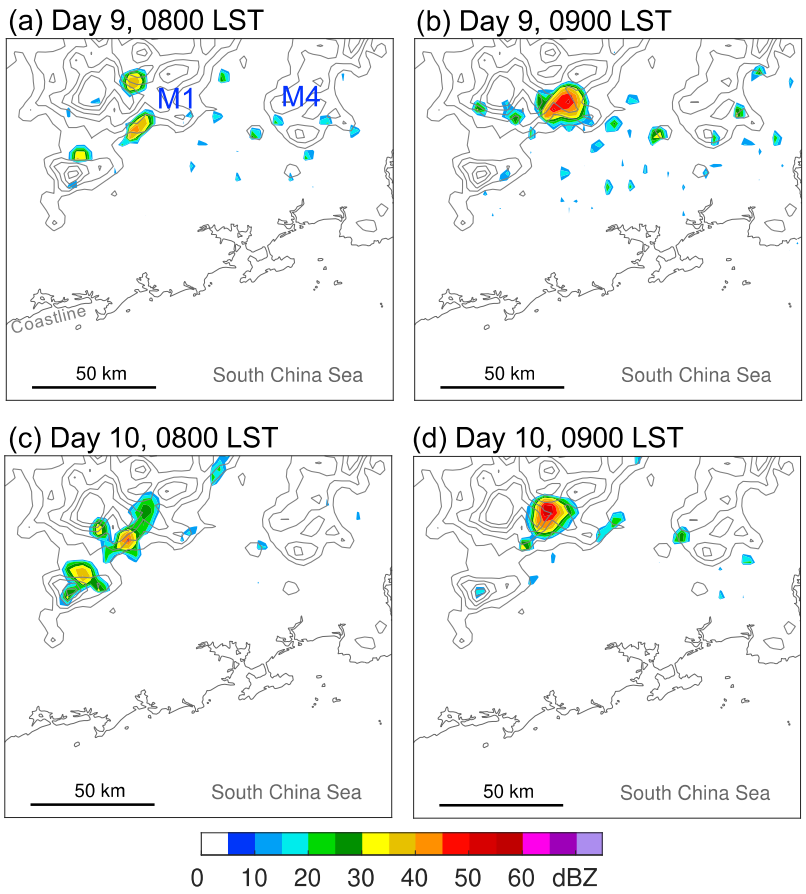

Figure 11. Maximum reflectivity at each vertical column obtained from the NO_TER experiment valid on (a),(b) day 9 and (c),(d) day 10. The terrain heights from 200 m to 950 m are contoured with an interval of 100 m. The major mountains labeled M1 and M4 are described in the text.

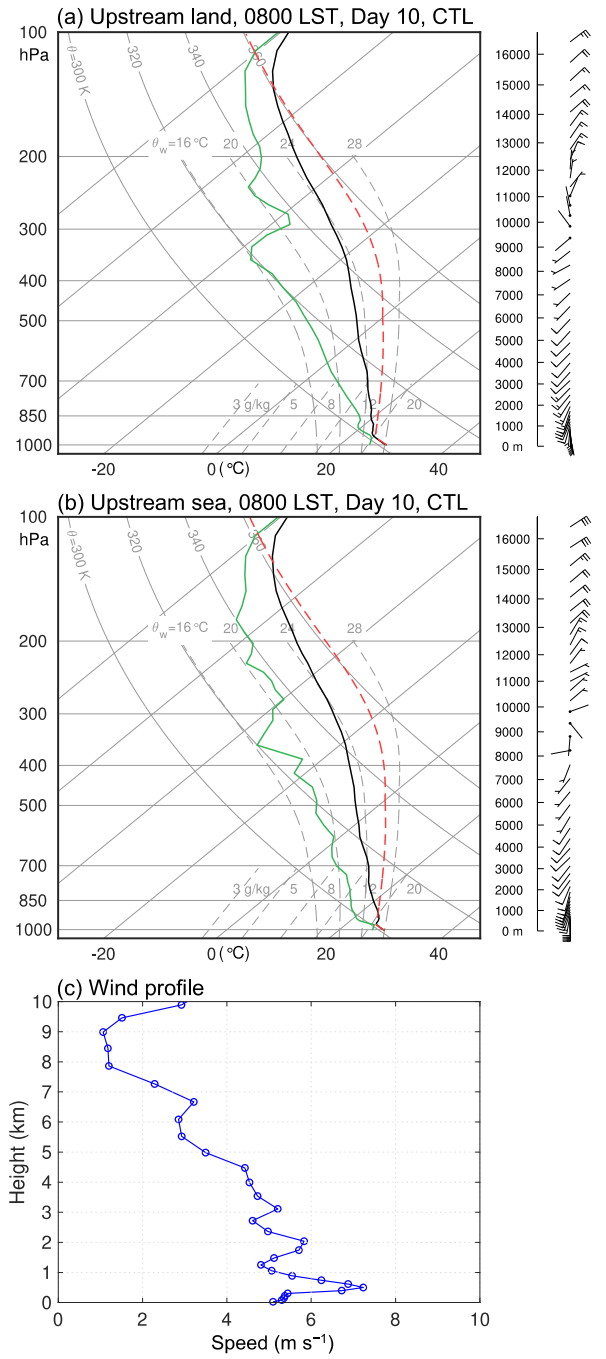

Figure 12. Skew *T*–log *p* diagrams showing the WRF soundings on the upstream (a) land and (b) sea of the mountain M2. The specific locations are denoted by the magenta and blue triangles in Figure 10c, respectively. The data are obtained from the CTL simulation at 0800 LST on day 10. The ambient temperature and dewpoint are represented by the solid black and green lines, respectively. The parcel that ascends undiluted from the surface is indicated by the dashed red line. The half barb and full barb represent 2 and 4 m s^{-1}, respectively. (c) Vertical wind profile of the sounding as shown in (b).

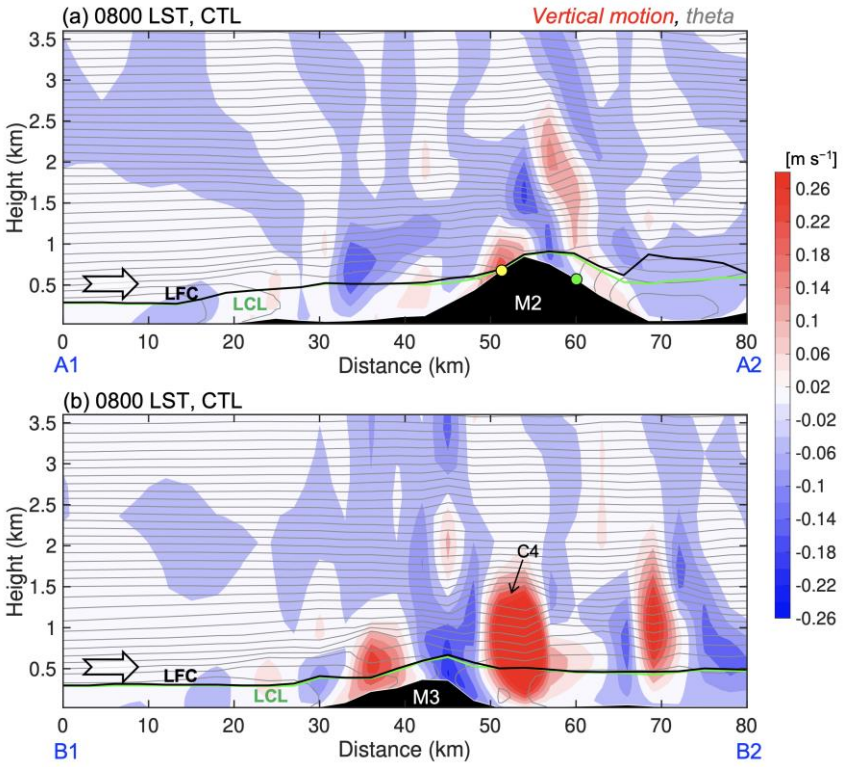

Figure 13. Vertical sections of isentropes (at an interval of 0.5 K) and vertical motions (shading) across the mountains (a) M2 and (b) M3 along the blue lines A1–A2 and B1–B2 in Figure 8j, respectively. The data are obtained from the CTL simulation at 0800 LST on day 10. The surface-based LCL (green curve) and LFC LCL (black curve) are also plotted for reference. The convective cell corresponding to the cell C4 in Figure 8j is labeled in (b). The black shading denotes the orography. The yellow and green dots in (a) denote the sounding locations as described in the text. The white arrow denotes the direction of the low-level flow.

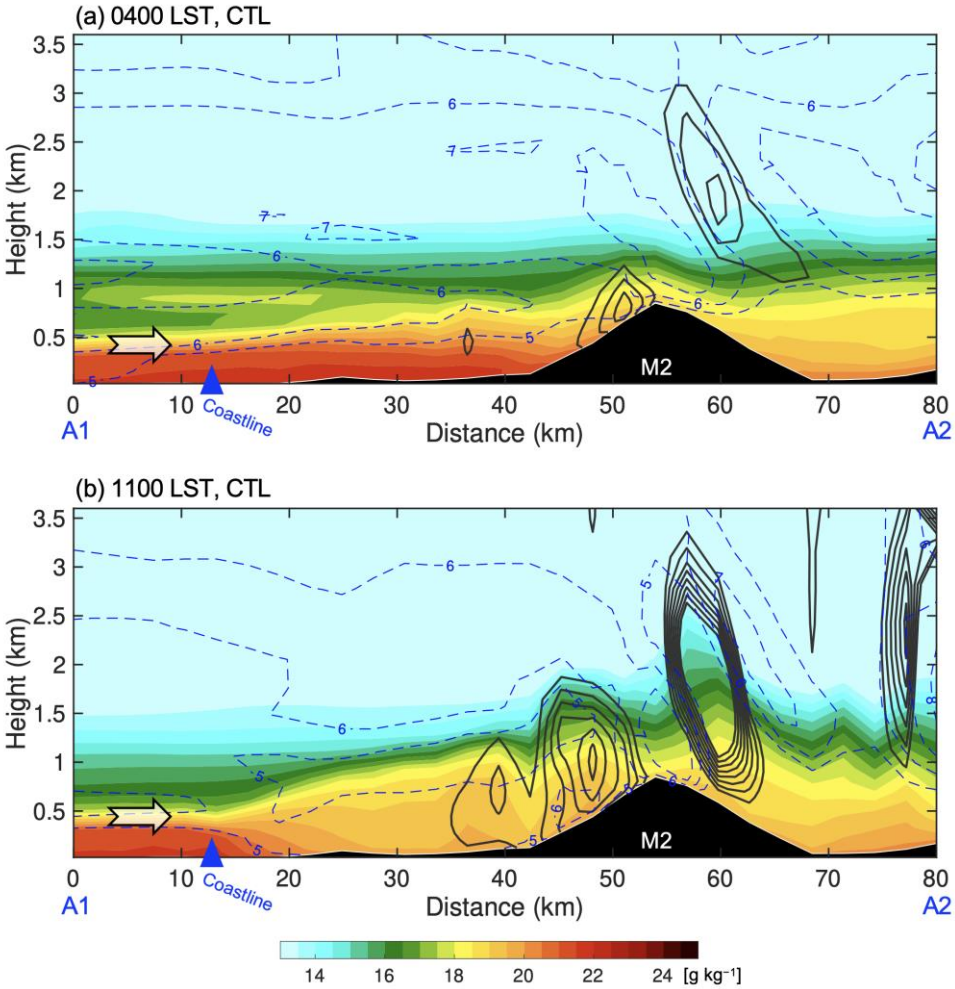

Figure 14. Vertical cross sections of water vapor mixing ratio (shadings), horizontal wind speed (contoured from 5 m s^{-1} in dashed blue), upward motion (contoured from 0.1 m s^{-1} at an interval of 0.1 m s^{-1}) for the CTL experiment at (a) 0400 LST and (b) 1100 LST. The white arrow denotes the direction of the low-level flow. The location of the cross section is denoted by the dashed line A1–A2 in Figure 8j. The blue triangle marks the rough location of the coastline.

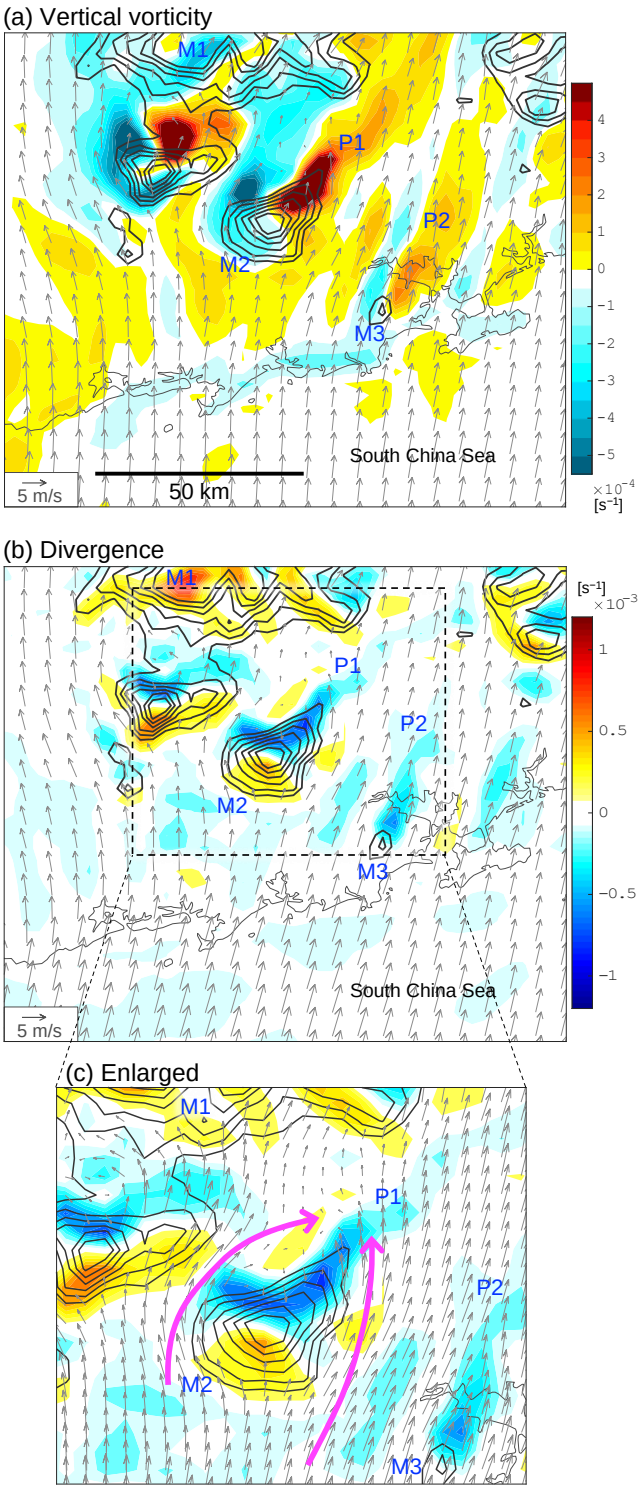

Figure 15. (a) Vertical vorticity (shadings) and horizontal winds (vectors) on the model level 5 above the ground valid at 0800 LST on day 10 for the CTL experiment. (b) Same as (a) but for divergence. The region within the dashed box is enlarged in (c). The magenta arrows indicate the flows passing around the mountain M2. The terrain heights from 250 m to 750 m are contoured with an interval of 100 m. The distance scale is presented at the bottom in (a).

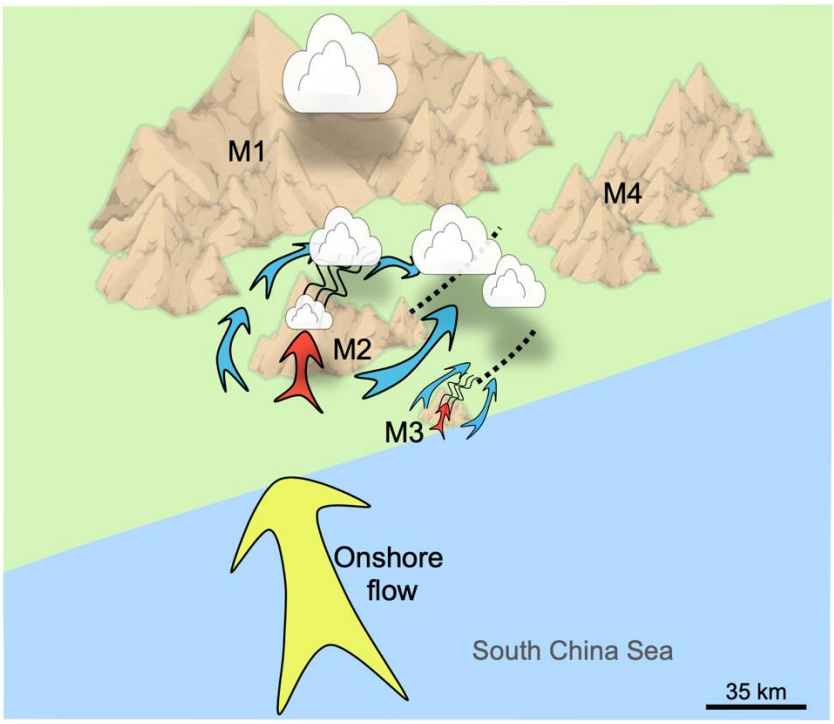

Figure 16. Schematic diagram depicting the low-level flows that pass around (blue) and over (red) the small-scale coastal mountains. The yellow arrow represents the low-level southwesterly onshore flow. The black curved lines denote the mountain waves induced by the flows that pass over the mountain ridges. The dotted lines represent lee-side convergence zones.